Mass Production of Calendering-Compatible Sulfur-Rich Secondary Particles via Hail-Inspired Nanostorm Technology for Advanced Metal-Sulfur Batteries

Lanxiang Feng
Sichuan University
Peng Yu
Sichuan University
Xuewei Fu
Washington State University
Mingbo Yang
Sichuan University
Yu Wang (yu.wang3@scu.edu.cn)
Sichuan University
Wei Yang
Sichuan University https://orcid.org/0000-0003-0198-1632

Article

Keywords: Metal-sulfur batteries, calendering-compatible sulfur-rich secondary particles, nanostorm technology, microenvironment management, thick sulfur electrode

Posted Date: December 2nd, 2020

DOI: https://doi.org/10.21203/rs.3.rs-110062/v1

Abstract

Scalable fabrication of high-quality thick sulfur electrodes with high-energy-density and good calendering-compatibility is a prerequisite for the practical success of metal-sulfur batteries. However, this task turns out extremely challenging due to the lack of not only advanced sulfur-rich active materials via scalable approach, but also quality-control principles for thick electrodes. Here, we first develop a new hail-inspired sulfur nanostorm (HSN) technology that can efficiently produce high-performance sulfur-rich secondary particles (S-rich SPs) with applesnail-egg-like structures. This biomimetic S-rich SPs rationally integrate critical material functions and good calendering-compatibility. Meanwhile, a concept of "healthy" microenvironment as learned from cell biology is proposed, for the first time, as a key principle revealing the critical role of calendering-compatibility in the quality-control of thick sulfur electrodes. Consequently, an ultrahigh areal capacity of 12 mAh cm^{-2} @ 1 mA cm^{-2} is realized. Further, we successfully demonstrate a pouch cell with an exceptional energy density of 430 Wh kg^{-1} or 1,004 Wh L^{-1} in a quasi-lean electrolyte condition. The technology and concept of this study may bring in new insights and general principles for design of advanced thick electrodes with, but not limited to, sulfur-based active materials.

Introduction

The high energy density and low cost of lithium-sulfur batteries are highly attractive for next-generation advanced energy storage devices.[1, 2] However, the broad implementations of lithium-sulfur batteries have been retarded by several challenges from both sulfur cathode and lithium metal anode.[3, 4, 5, 6] Particularly for sulfur cathode, there are a number of critical issues coupled together. Namely, the dissolution of lithium polysulfides (LiPSs) is associated with notable volume change of active materials, and shuttle effects and structural instability of LiPSs. To address these issues, extensive efforts have been focused on designing conductive and functional host materials for sulfur cathode to realize good electronic conductivity, trap LiPSs and suppress the shuttle effect.[7, 8, 9] For example, various carbon-based nanomaterials, such as graphene,[10, 11, 12] carbon nanotubes,[13, 14] core-shell nano-carbon,[15, 16] have been extensively studied in the past decade. Recently, catalysts for fast LiPSs conversion were proposed as another effective strategy for suppressing LiPSs diffusion and shuttle effects.[17, 18, 19] These efforts are critical for fundamental understanding of lithium-sulfur electrochemistry, and design principles for sulfur active materials. However, satisfactory electrochemical performance was usually realized on the premise of a very limited sulfur loading, which led to a much lower energy density than that of current commercial Li-ion batteries (4 mAh cm^{-2}).[20]

To overcome the hurdles for practical applications, it is necessary to boost the sulfur loading in thick electrode configuration. Unfortunately, this task has been proved very difficult due to not only the deterioration of the well-known issues above, but also new challenges of thick electrodes from scalable fabrication, quality control principles, and failure mechanisms and so on. Specifically, the first challenge on electrode particle level is how to massively fabricate high-performance sulfur active materials with

desired material functions for addressing the above well-known issues. Conventional strategies based on solution methods are usually difficult or costly to scale up.[21] At the same time, the sulfur content needs further improvement to be above 70 wt% to achieve high energy density.[22, 23] The second challenge on composite level is how to realize thick sulfur electrodes with crack-free and uniform microstructures. This challenge is linked to many factors, including the characteristics of active electrode particles, electrode compositions and slurry formula, binder properties, fabrication conditions and so on.[24] To conquer this challenge, Yan et. al.,[25] proposed advanced functional binder using the polar amino groups by the polymerization of hexamethylene diisocyanate with polyethylenimine polymer. Binder-free electrodes based on conductive 3D scaffolds, such as carbon nanobute or nanofiber fabrics,[13, 26, 27, 28] have also been proposed to fabricate flexible thick electrodes. The third challenge, and probably the most difficult one, is how to stabilize the structures and functions of thick sulfur electrodes during their manufacturing and practical operation. In particular, calendering process is an essential step of electrode fabrication. It helps improve the structural stability, interface quality and energy-density of the whole electrode. Specifically, it is a crucial step to shape and stabilize the assembling structures of the final composite electrodes, including electron-transport-network (ETN) assembled by conductive agent, and ion-transport-network (ITN) assembled by pores and voids.[24] However, since sulfur is typically a soft material, the assembling structures, usually the ITN structure, can be easily destroyed by calendering as revealed by Xiao et. al.[29] In addition, for thick sulfur electrode, ETN and ITN structures can also be destroyed by solid-liquid or liquid-solid conversion of active materials during charging/discharging as revealed recently by Liu et. al.[30] Therefore, future efforts should be more focused on improving the calendering-compatibility of sulfur active material, and so the assembling structures of the composite electrodes, in addition to the material functions for relieving the issues of LiPSs dissolution and shuttle effects.

To address the above issues and challenges of thick sulfur electrodes, it is important to learn from commercial lithium-ion-batteries (LIBs), which usually employ hard active materials, such as $LiCoO_2$, $LiFePO_4$ etc. Especially, to further improve the energy density, high-capacity active materials, such as lithium-rich metal oxide particles, are usually fabricated into hard spherical secondary particles.[31, 32, 33] Therefore, it is concluded that the design and fabrication of sulfur-rich secondary particles (S-rich SP) via a scalable approach will be the key towards the commercialization of high-performance and long-life thick electrodes.[29, 34, 35] Importantly, to protect the ETN and ITN structures of the electrode during both calendering process and practical applications, the S-rich SPs need a synchronous fulfilment of good mechanical properties and material functions of trapping LiPSs and conducting ions/electrons. However, to our best knowledge, this concept of S-rich SP has not been proposed yet.

Herein, inspired by the hail formation mechanism, we report a biomimetic design and scalable production of sulfur-rich secondary particles (sulfur SP) by hail-inspired nanostorm technology (sulfur SP@HSN) to address the above mentioned challenging issues in thick sulfur electrode. As illustrated in Fig. 1a, the hail formation process proceeds in several steps and conditions: water evaporation at high temperatures, liquid condensation onto solid dust surface, aggregation and solidification with low temperature condition. Based on the understanding of this process, we develop a simple high-speed shearing strategy

for compositing sulfur, conductive nanomaterials (core-shell Ketjen black, for instance) and LiPSs nano-catalyst as shown in Fig. 1b. Via this strategy, applesnail-egg-like sulfur SPs can be massively produced via a process similar to that of hail formation (see Fig. 1c).

There are several significant advantages for the above strategy. Firstly, material functions, including trapping and catalysis of LiPSs and accommodation of volume change, have been integrated into the hard and biomimetic secondary particles, which can bring SP with good structural stability and thereof function stability during calendering or cycling process. Secondly, the size and composition of the SP can be designed on demand to further improve the structure stability and electrochemical performance. Finally, the entire process is solvent-free and easy to scale up. For example, as demonstrated in Fig. 1c, we were able to composite 400 g bulk sulfur with 98 g carbon nanomaterials and 2 g Co_2O_3 in only 5 min, corresponding to a production rate of 100 g/min. The above hard biomimetic sulfur SP@HSN finally can benefit the resultant electrode composite with high sulfur-loading, stable and uniform ETN and ITN structures even after calendering process. Furthermore, we successfully assembled pouch-cells with various high S-loading electrodes delivering the highest gravimetric energy density (E_g) about 430 Wh/kg and volumetric energy density (E_v) of 1004 Wh/L. It is believed that the above design and mass production of sulfur SP makes an important leap towards the practical success of Li-S batteries.

Result And Discussion

Here we present that hollow nano-size conductive agent (Ketjenblack (KB), **Figure S1a**), sulfur blocks (**Figure S1b**) and nano-Co_2O_3 (**Figure S1c**) can be easily composited into microscale sulfur SPs by the above hail-inspired sulfur nanostorm (referred as SP@HSN below). For comparison, sulfur blocks were also composited with KB and Co_2O_3 by conventional high-temperature melt-diffusion method, and the sample was designated as sulfur AP@HTM. As shown in Fig. 2a the sulfur AP@HTM shows an irregular particle size/shape with a poor coverage of KB against sulfur. In contrast, it is observed that the sulfur SP@HSN shows applesnail-egg-like morphology in Fig. 2b. The structures of sulfur SP@HSN was further characterized by TEM image. Figure 2c reveals that sulfur is encapsulated in partially open hollow KB nano-host (**Figure S2**). Meanwhile, a number of Co_2O_3 nanoparticles (see Fig. 2c) are embedded inside the sulfur SP@HSN. Elemental mapping (see Fig. 2d) further confirms that S, C and Co elements are uniformly dispersed throughout the sulfur SP@HSN composite particle. To further investigate the S/C interactions, the nitrogen adsorption-desorption testing was conducted. As shown in Fig. 2e and **Figure S3a**, the specific surface area of sulfur SP@HSN-5 min sample is 3.2 $m^2 g^{-1}$, which is far less than that of KB (1400 $m^2 g^{-1}$), indicating that the porous KB was impregnated by sulfur. Besides, the specific surface area of different S/KB samples is summarized in **Table S1**. Generally, larger size of SP possesses smaller specific surface area that needs a less amount of electrolyte for wetting, thus boosting the gravimetric energy (Eg) of Li-S batteries.[36] However, both sulfur AP@HTM and sulfur SP@HSN particles show similar pore distribution in the range of 5 nm-100 nm (**Figure S3b**), which is probably related to the stacking pores inside the sulfur SP@HSN. These stacking pores will provide ion-transportation channels inside the secondary particles. The S/C binding interactions were further investigated by the first heating

curve of differential scanning calorimetry (DSC) at a scan rate of 10 ^{o}C/min. As shown in Fig. 2f, two sharp melting peaks are observed for pure sulfur. In contrast, sulfur SP@HSN presents a single and very weak melting peak as compared with pure sulfur and sulfur AP@HTM. This result further confirms that sulfur is well-confined inside the nano-channels or pores of KB via a vapor-deposition process as demonstrated in Fig. 1b. In other words, the sulfur SP@HSN shows the strongest sulfur/C binding interactions benefited from the hail-inspired sulfur nanostorm technology. Thermogravimetric analysis (TGA) as shown by Fig. 2g reveals that the sulfur content in sulfur SP@HSN composites is 80%, which confirms the S-rich feature of the secondary particles and is consistent with the formula before the compositing.

In addition to the above design flexibility in composition, the size of the sulfur-rich secondary particles can be controlled easily by compositing time. The size of active electrode particles is actually a very critical factor controlling not only the energy density, but also the quality of the final composite electrodes. In particular, it shapes the electrode assembling structures (ion-transport network (ITN) and electron-transport network (ETN)) as introduced previously. Rational size of the active particles is also critical for preparing uniform and crack-free thick electrode.[2, 29] Fig. 2h shows that the particle size can be easily regulated by the compositing time. When the compositing time is only 2 min, the particle size of sulfur SP@HSN mainly concentrates in the range of 1–10 um, as shown in the top of Fig. 2h. As the compositing time increased to 3 min or 5 min, the particle size further increased (see **Figure S4**). According to the compositing time, the samples are defined as the sulfur SP@HSN-3 min (see the middle of Fig. 2h) and sulfur SP@HSN-5 min (see the bottom of Fig. 2h). For these sulfur SP@HSN particles, one can clearly find that they are secondary particles with tightly stacked nanoscale S/KB particles. In practice, the tap density of active particles is widely employed as a parameter to indicate their E_v potential in final electrodes. A high tap density of electrode particles will favor the fabrication of compact electrodes with high E_v.[37]. From the Fig. 2i, the sulfur SP@HSN-5 min sample can reach a high tap density around 0.83 g cm^{-3}, which is higher than even pure sulfur particles (0.724 g cm^{-3}), and much higher than sulfur AP@HTM sample (0.53 g cm^{-3}). This tap density is at the same level of commercial Si/C secondary particles (0.8 g cm^{-3}). The results indicate that such a secondary particle is favorable to boost the volumetric-energy-density (E_v) of electrode.

Mechanical properties of S-rich secondary particles are among the foremost properties considering their practical applications. It is important to understand the roles of mechanical properties of active materials (AMs) in controlling the overall quality of the final composite electrodes, which is seldom discussed in literature to our best knowledge. Here, we attempt to understand the mechanical properties of electrodes and their evolution during manufacturing. Firstly, electrode calendering is a well-known essential process that has complicated impacts on the electrode quality and energy density. Therefore, the mechanical properties of individual AM particles have to be strong enough to maintain its structure integrity and the structural stability of the electrode composite. Probably because classic electrode particles, such as $LiCoO_2$ and $LiFePO_4$, are hard inorganic materials, the AM mechanical properties are usually not an obvious issue. However, for new high-capacity electrode materials, such as sulfur and lithium metal, the

situations are totally different. To dig out the fundamental principles, we introduce a concept of AM microenvironment below.

The concept of microenvironment in cell biology indicates significant influences on cell metabolism and division. As illustrated in Fig. 3a, the cell exchanges complicated nutrients and signals through the surrounding micro-vessels and neural network, which are the essential physical structures of the cell microenvironment. Similar to this picture in cell biology, the AM particle can also be viewed as an electrochemical micro-cell with its own microenvironment. As illustrated in Fig. 3a, the electron-transport-network (ETN) built by conductive nanoparticles, and the ion-transport-network (ITN) built by pores or voids together generate the physical structures of AM microenvironment for supporting charge (ions and electrons) transport during electrochemical reactions. Similar to the cell microenvironment, the electrochemical performance of individual micro-cells (AM particles) should be dependent on the detail physical structures and their function stability during cycling. Therefore, to regulate and stabilize the AM microenvironment in practical conditions is of great significance for high-performance energy storage devices, but is a challenging task for high specific capacity AMs such as sulfur, silicon and lithium metal.

From the AM microenvironment point of view, the calendering processing not only smoothies the electrode surface, but also shrinks the volume fraction of microenvironment (mainly the ITN part), improving the energy density by decreasing the electrolyte/AM ratio.[29, 36, 38] At the same time, calendering is also a critical process regulating the physical structures and structural stability of the AM microenvironment and its assembling structures, that is, the entire ETN and ITN on the electrode level. In this case, the mechanical property of AM is critical for the structural evolution of microenvironment. As illustrated in Fig. 3b, for conventional electrode particles, such as $LiCoO_2$, $LiFePO_4$ etc., they are very hard materials. Therefore, the physical structures of AM microenvironment are mainly controlled by the stacking of AM and conductive agent particles under the compression force during calendering or device assembling. As long as the AM particles stack closely enough to reach a force equilibrium point against the compression, they finally form a strong network to mechanically protect the AM microenvironment, and the INT and ENT on the whole. Therefore, for thick sulfur cathode, the AM particles have to be hard enough or calendering-compatible to achieve a supportive AM microenvironment for efficient ion/electron conduction as illustrated in Fig. 3b. Unfortunately, it has been a big challenge to fabricate calendering-compatible S-rich AM particles. Therefore, the microenvironment issues come from the very beginning of electrode fabrication. As illustrated by Fig. 3c, most of S/C composite particles are weak due to the softness of sulfur in nature, such as the sulfur AP@HTM sample introduced in this study. In this case, calendering process can easily shape the AM particles into a closed stacking configuration, and crush the ITN microenvironment, leading to poor electrolyte wetting. In fact, the above microenvironment issues are not unique to sulfur cathode. With the intensively increasing interests on high-energy-density rechargeable batteries, most of the challenging issues of high-capacity AMs are actually from the microenvironment. For instance, the big volume change of silicon anode can easily destroy its ETN microenvironment, although silicon is a hard material. Therefore, microenvironment issues are generally

found in various battery systems and throughout their service life. “Healthy” microenvironment will play a more and more important role in understanding the performance of next-generation LIBs and beyond.

For the sulfur SP@HSN particles, we have particularly investigated their significant advantages in fabrication of thick electrodes with an emphasis on the good calendering compatibility. Firstly, the microenvironment quality of the composite electrodes before calendering treatment was examined for samples with different S-loadings. For the control sample, sulfur AP@HTM, as shown in Fig. 3d, Fig. 3e and **Figure S5a**, many cracks can be observed when the S-loading is around 5 mg cm^{-2}. The sulfur AP@HTM even automatically detaches from the Al-foil when the S-loading reaches to 10 mg cm^{-2} (**Figure S6a**). In contrast, the sulfur SP@HSN electrode with 5 mg cm^{-2} S-loading (Fig. 3h, Fig. 3i and **Figure S5b**) displays uniform and crack-free surface. Furthermore, even with S-loading of 15 mg cm^{-2}, there is no visible crack for the sulfur SP@HSN-5 min electrode (**Figure S6b**). Electrode cracks can be viewed as uncontrollable big microenvironment defects, which can lead to structural non-uniformity and instability, and thereof non-uniformity of ion and current flux. The above structural differences convincingly confirm that the sulfur SP@HSN effectively improves the microenvironment quality with much better uniformity, even at a high S-loading level.

Importantly, the sulfur SP@HSN active material also demonstrates good calendering compatibility. To investigate the calendering compatibility, the sulfur AP@HTM and sulfur SP@HSN electrodes with S-loading of 5 mg cm^{-2} were calendered at different pressures and temperatures. Figure 3f shows the electrode surface morphology for sulfur AP@HTM sample after treatment by 4 MPa at 40 ^{o}C. One can find that most of the AM is deformed and the majority of the pores disappear. Furthermore, when the AP@HTM electrode was compressed with 4 MPa at 80℃, the sulfur AP@HTM particles almost deformed into a compact sheet without porous structures (Fig. 3g and **Figure S7c**). This behavior even happened at a lower temperature around 60 ℃ (**Figure S7b**). In contrast, for the sulfur SP@HSN electrode, a much better calendering compatibility was confirmed at different temperatures. The particle shape and pores between particles survived at 4 MPa even at 80 ℃ (Fig. 3j, Fig. 3k, **Figure S7d, Figure S7e** and **S7f**). The good calendering compatibility at different temperatures indicates that the sulfur SP@HSN is not only mechanically strong, but also effective to confine the sulfur in the KB host at high temperatures. The good mechanical property is likely due to the unique applesnail-egg-like structures with uniformly dispersed hard Co nanoparticles inside. The good calendering compatibility of sulfur SP@HSN means good mechanical properties of the SP@HSN particles. To directly investigate the mechanical properties of sulfur SP@HSN, Atomic Force Microscopy (AFM) probe was randomly performed onto the AM particle as shown by the inset in Fig. 3l. The sulfur SP@HSN sample shows an average apparent Young’s modulus of 5.3 MPa, which is much higher than 4.2 MPa for the control sample. It is noted that this apparent Young’s modulus is not the real modulus of the individual AM particles that is difficult to test. However, it is a useful parameter describing the collective mechanical behavior of the AM particles, which provides critical information for choosing rational compression pressure during calendering processing.

To further study how the microenvironment structures change with compression pressure, the dependence of electrode porosity and thickness on compression pressure was systematically studied for the SP@HSN electrode in comparison with its control sample. Specifically, for the control sample, sulfur AP@HTM electrode, the thickness changes from 210 um to 50 um when the pressure increased from 0 MPa to 30 MPa. For the sulfur SP@HSN electrode, the electrode thickness changes from 207 um to 70 um at the same compression condition (**Figure S8**). At the same time, the electrode thickness of AP@HTM is much more sensitive to the compression pressure, as compared with that of SP@HSN electrode sample. This result indicates that the spherical SP@HSN helps to form more compact and strong stacking structures during electrode fabrication. Meanwhile, the electrode porosity was also recorded after treatment by different compression pressures. For the SP@HSN electrode, its porosity decreased from 60–40% when the pressure increased from 0 to 30 MPa (Fig. 3m). While, for sulfur AP@HTM electrode, the porosity dropped remarkably from 64–29% at the same condition.

The electrode porosity is a collective parameter describing the total volume fraction of the ion-transport-network (ITN) microenvironment. To build the final ITN, all the pores are filled by liquid electrolytes. Therefore, the liquid electrolyte wetting behavior can also reflect the ability of microenvironment to establish ion-conduction networks around the AM particles. As shown in **video S1** and **video S2**, the sulfur SP@HSN electrode after 4 MPa calendering shows a faster wetting process than that for sulfur AP@HTM electrode, indicating that the sulfur SP@HSN electrode has better ITN microenvironment. The cross-section SEM images of sulfur AP@HTM and sulfur SP@HSN electrode before and after 4 MPa treatment further confirm the above results (**Figure S9)**. As important as that of the ITN, the ETN part of the microenvironment controlling the electronic conduction is mainly determined by the dispersion of conductivity agent and the electronic contact between two different AM particles. To probe ETN part of the microenvironment, Fig. 3n shows the surface resistivity evaluated by conductive micro-probe at 20 different location of the electrode surface. One can find that the resistance and deviation for sulfur SP@HSN electrode is much less than that of sulfur AP@HTM electrode. Such a result indicates that the sulfur SP@HSN helps to form uniform ETN microenvironment across the whole electrode.

From the above results, one can find that the biomimetic S-rich secondary particles (SP@HSN) show several significant advantages in low-cost fabrication of high-quality thick sulfur-electrodes. Especially, all these advantages are fundamentally linked to the capability of microenvironment control during the manufacturing as well as the electrochemical cycling. In order to further investigate the electrochemical performance, the resultant S-cathodes with various sulfur loading were first evaluated with a coin cell using electrolyte/sulfur (E/S) ratio of ~ 10 ul mg^{-1}. As shown as in Fig. 4a, the sulfur SP@HSN electrode with a sulfur loading of 2 mg cm^{-2} delivers a high discharge capacity of 1356 mAh g^{-1} at current density of 0.1C, it further delivers discharge capacity of 1019, 877, 760, and 639 mAh g^{-1} at current density of 0.2, 0.5, 1 and 2C, respectively, exhibiting an excellent rate capability. Moreover, the voltage profile in **Figure S10** shows flat and long plateaus with low polarization even at high current densities, indicating good ITN and ETN in the sulfur SP@HSM electrode. On the contrary, the sulfur AP@HTM electrode (Fig. 4a) delivers obviously lower capacity of 1011, 712, 601, 522 and 430 mAh g^{-1} at the current density

of 0.1, 0.2, 0.5, 1, and 2C, respectively. Nyqusit plot also shows that the sulfur SP@HSN electrode has a smaller equivalent electrical circuit (R_0) and charge transfer resistance (R_{ct}) (**Figure S11**) as compared with the control sample, further verifying that the sulfur SP@HSN electrode has a more efficient ITN and ETN microenvironment, thus leading to an excellent rate capability. Furthermore, the cycling performances of sulfur AP@HTM and sulfur SP@HSN electrodes with same sulfur loading of 5 mg cm^{-2} at a current density of 0.5C were compared in the Fig. 4b. After two cycles of activation at a current density of 0.1C, the sulfur SP@HSN electrode achieves a high initial capacity of 802 mAh g^{-1} with good capacity retention of 66% over 110 cycles. In comparison, the sulfur AP@HTM electrode shows rapid capacity decay from 679 to 297 mAh g^{-1}, indicating a low sulfur utilization and severe “shuttling effect”.

Generally, for practical Li-S batteries, it is critical to develop electrodes with area capacity at least comparable to that of current LIBs. As shown in Fig. 4c, the sulfur SP@HSN electrode with 5 mg cm^{-2} delivers a maximum areal capacity of 4.1 mAh cm^{-2} at a current density of 0.5C. After 55 cycles, a reversible areal capacity of 3 mAh cm^{-2} was still obtained, which is lower than that for the practical level of commercial LIBs (~ 4 mAh cm^{-2}), but much higher than the level reported in most of the literatures (~ 2 mAh cm^{-2}). Therefore, to demonstrate its superiority in energy-density as compared with current commercial LIBs, we further prepared thicker electrodes with 8.1 and 9.7 mg cm^{-2} of sulfur. These thick electrodes deliver areal capacity of 5.3 and 7.5 mAh cm^{-2} at a current density of 0.2 C, respectively, which is much higher than that of the commercial LIBs. To further investigate its possible application in super-high energy density batteries, the sulfur loading was even increased to 14.1 mg cm^{-2}. As shown by Fig. 4d, a super-high area capacity of 16.5 mAh cm^{-2} was achieved at a low current density of 0.5 mA cm^{-2} for this super-high S-loading electrode. Finally, a stable areal capacity (~ 12 mAh cm^{-2}) at a current density of 1 mA cm^{-2} was realized over 28 cycles, indicating its promising application in low-cost high-energy-density metal-sulfur batteries.

The above success in coin cells is a good indication that the calendering-compatible biomimetic SP@HSN is able to deliver a high specific capacity even at a high S-loading condition in thick electrodes. It is noted that the good electrochemical performance of the SP@HSN electrode is fundamentally contributed by the ITN and ENT microenvironment as introduced previously. In other words, the superiority in microenvironment control by the SP@HSN in practical conditions is one of the most critical reasons for its good electrochemical performance. To test this advantage in large scale electrodes, pouch-cells with size of 4.7 cm · 7.7 cm were assembled based on various sulfur loading for the sulfur SP@HSN electrodes. At the same time, a low E/S ratio of ~ 4 ul mg^{-1}, was used as demonstrated in the Fig. 5a. All the pouch-cells based on various sulfur loading of cathodes from 5 mg cm^{-2} to 12 mg cm^{-2} exhibited a high discharge specific capacity and good cycling stability (**Figure S12a**). Meanwhile, all the voltage profiles of pouch-cells (**Figure S12b-Figure S12d**) are almost identical to those of coin-cells and the average discharge voltage is around 2.1 V even after several cycles, suggesting a lower polarization and a good health state of cell. Specifically, Fig. 5b shows that the pouch-cell with a high sulfur loading of 12 mg cm^{-2} delivers a high discharge capacity of 1294 mAh g^{-1} at a current density of 0.02C and

exhibits a cycling performance over 10 cycles. Subsequently, the energy density of pouch-cell was evaluated by a simplified model based on Eq. 2 and Eq. 3. As shown in Fig. 5c, our pouch-cell with an E/S ratio of 4 ul mg^{-1} and sulfur loading of 12 mg cm^{-2} shows a high joint E_g (430 Wh kg^{-1}) and E_v (1002 Wh L^{-1}) at 0.02C and good cycling stability. Such an energy-density level is much higher than the commercial LIBs and the Li-S batteries reported by most of the literatures,[35, 39, 40] as shown in Fig. 5d. It is noted that optimization of mass loading, E/S ratio and other important parameters could be employed to further boost the energy density of pouch-cell.[23] For instance, if we further decrease the E/S ratio to 3 ul mg^{-1}, the energy density of the pouch-cell can improved to be above 500 Wh kg^{-1}, the goal set by the Department of Energy, USA.

It is noted that the above performance for the calendering-compatible biomimetic SP@HSN electrodes was achieved without additional efforts on electrolyte, binder, separator and lithium anode. The high specific capacity, areal capacity and good cycling stability of sulfur SP@HSN electrode with super-high loading is likely contributed by the following factors. 1) The biomimetic design of the SP@HSN sulfur active material with a hard core-shell structure can help to suppress the shuttling of LiPSs as illustrated in Fig. 1c, which has been widely reported in literature.[29, 35, 41] 2) The good calendering-compatibility of the SP@HSN can help to build a “healthy”, stable and uniform ITN/ETN microenvironment even for thick and large-scale electrodes. This is critical for the capacity extraction of individual AM particles. 3) The uniform ITN/ETN microenvironment finally assembles into uniform ITN/ENT structures on large-scale electrode level, especially for thick electrode. This can remarkably alleviate the formation of Li_2S/Li_2S_2 precipitates on the interface between cathode and separator, greatly improving the cycling stability of Li-S batteries. 4) A uniform ITN/ETN microenvironment and its assembly structures on electrode level can help to generate uniform Li^+-flux onto the lithium metal side that is beneficial to stabilizing Li metal as well.

Conclusion

In summary, In order to do make a leap towards the practical success of metal-sulfur batteries, such as lithium-sulfur batteries, we focus on the essential tasks from both technical and scientific sides of scalable fabrication of high-quality thick sulfur cathode. Firstly, learning from successful conventional electrode materials, we introduce the concept of calendering-compatible S-rich secondary particles (S-richSPs) for fabrication of high-energy-density thick sulfur electrodes. The S-rich SPs has to be well-designed to combine good mechanical properties with desired functions. Secondly, to massively produce the designed S-rich SPs, we further develop a novel hail-inspired sulfur nanostorm technology, which is totally solvent-free and industry-friendly. Thirdly, for an in-depth understanding of the significance of good calendering-compatibility in controlling the quality of thick sulfur electrodes, we further proposed the concept of “healthy” microenvironment in composite electrodes, which fundamentally controls the ion/electron transport for the AM. Finally, the promise of the S-rich secondary particles by the above nanostorm technology (SP@HSN) has been successfully demonstrated by high-energy-density Li-S batteries in both coin cell and pouch cell configuration. As a result, the sulfur SP@HSN electrode with a

super high loading of 14.1 mg cm^{-2} stably delivered an areal capacity of 12 mAh cm^{-2} at a current density of 1 mA cm^{-2}. At the same time, pouch cells based on various sulfur loading of sulfur SP@HSN electrodes were fabricated, which delivered a high energy density of 430 Wh kg^{-1} (1004 Wh L^{-1}). In short, this study will shed the light on rational design, scalable fabrication and fundamental understanding of advanced S-rich secondary particles for high-energy-density metal-sulfur batteries, which should be instructive for other batteries and supercapacitors.

Declarations

Author contributions

L. F., W. Y., and Y. W., conceived and designed this work. L. F., P. Y., and X. F., performed the experiments and measurements. M. Y., W. Y., and Y. W., revised this manuscript. L. F., and Y. W., wrote this paper with input from other authors. All the authors discussed the results.

Acknowledgements

This research is sponsored by the Double First-Class Construction Funds of Sichuan University and National Natural Science Foundation of China (NNSFC). The authors thank Prof. Qiang Zhang (Tsinghua University) and Prof. Wei-Hong Katie Zhong (Washington State University) for their helpful discussion and suggestion. The authors also would like to thank Prof. Yanhua Niu and her group (Sichuan University) for the help on assembling coin-cells.

Experimental

Synthesis of sulfur AP@HTM and sulfur SP@HSN: 98 g KB and 2 g Co_2O_3 was ground with 240 g sulfur powder to form a homogenous mixture. The mixture was transferred into a Teflon-line stainless reactor and heat treated for 12 h at 155℃, generating sulfur AP@HTM sample via melt-diffusion method. The same mixture was transferred to a sealed stainless reactor and stirring for 5min at room temperature, obtaining the sulfur SP@HSN via high-speed shearing strategy as demonstrated in **Figure 1b**.

Synthesis of sulfur AP@HTM and sulfur SP@HSN electrode: the sulfur SP@HSN active material was mixed with carbon black, gelatin-modified PAA binder in mass ratio of 80:10:10 to prepare the electrode slurry. Then, the electrode slurry was then coated onto an Al foil and vacuum dried for 12h at 60 ℃. The sulfur AP@HTM electrode was prepared for comparison, using the same mass ratio and drying condition.

Materials Characterization: The morphologies were investigated by SEM (FESEM, Japan) with energy-dispersive X-ray analysis (EDX) and TEM (JOEL2010F). The microstructures and pore size distribution of particles were characterized by Nitrogen adsorption/desorption isothermal (ASAP 2020 HD Analyzer). The electronic conductivity was obtained by a standard four-point-probe resistivity measurement system. Thermogravimetric analyses (TGA, Q600, TA instrument, USA) were used to measure the sulfur content.

Atomic Force Microscopy (AFM) probe (Bruker Corporation; Santa Barbara, CA) was conducted to obtain the Young's modulus of APs/SPs particle films. The sulfur binding capacity of obtained samples were investigated by differential scanning calorimetry (DSC) Q20 (TA Instruments, Milford, MA, USA) under a nitrogen atmosphere at the scan rate of 10 ^{o}C/min.

Electrochemical characterization: Coin-cells (CR2032) were fabricated using sulfur AP@HTM or sulfur SP/HSN active materials, Li metal anode and the Celgard 2325 separator. For the pouch-cells, the size of cathodes is 7.7 cm ´ 4.7 cm. The electrolyte used was 1 M lithium bis(trifluoromethanesulfonyl) imide (LiTFSI) dissolved in a mixture of 1,3-dioxolane and dimethoxyethane (1:1 in volume) with 1% addition of $LiNiO_3$ additive. All cells were performed by Neware Battery measurement system with a voltage range of 1.7-2.8V (vs. Li/Li^+) at 25℃. Electrochemical impedance spectra (EIS) were tested on electrochemical instrument (ChenHua, Shanghai) in the frequency range from 0.1 to 10^6 Hz.

The evaluation of electrode porosity: the electrode porosity was evaluated by the n-butanol uptake, as shown in Equation 1.

$$\text{Electrode porosity} = \frac{\frac{m1}{\rho 1}}{(\frac{m1}{\rho 1} + \frac{m2}{\rho 2})} \times 100\% \qquad (1)$$

Where m1 and m2 are the weight of n-butanol and electrode, ρ1and ρ2 are the density of n-butanol and electrode, respectively.

The evaluation of energy density: the E_g and E_v were calculated from Equations (2) and (3), respectively.

Where E_g and E_v are the gravimetric energy density (Wh kg^{-1}) and volumetric energy density (Wh l^{-1}), respectively, V is the output voltage of pouch-cell (2.1V), C is the areal capacity of pouch cell (mAh cm^{-2}) , Mi and Ti are the mass per unit square (mg cm^{-2}) and the thickness (cm) of the whole pouch cell but the Aluminum soft packaging film.

$$Eg = \frac{VC}{\sum Mi} \qquad (2)$$

$$Ev = \frac{VC}{\sum Ti} \qquad (3)$$

References

1. Manthiram, A., Fu, Y. Z., Chung, S. H., Zu, C. X., Su, Y. S. Rechargeable lithium-sulfur batteries. *Chem. Rev.* **114**, 11751–11787 (2014).

2. Choi, J. W., Aurbach, D. Promise and reality of post-lithium-ion batteries with high energy densities. *Nat. Rev. Mater.*, **1**, (2016).
3. Cuisinier, M., Hart, C., Balasubramanian, M., Garsuch, A., Nazar, L. F. Radical or Not Radical: Revisiting Lithium-Sulfur Electrochemistry in Nonaqueous Electrolytes. *Adv. Energy Mater.* **5**, 1401801 (2015).
4. Wang, Q., *et al.* Direct Observation of Sulfur Radicals as Reaction Media in Lithium Sulfur Batteries. *J. Electrochem. Soc.* **162**, A474-A478 (2015).
5. Suo, L. M., Hu, Y. S., Li, H., Armand, M., Chen, L. Q. A new class of Solvent-in-Salt electrolyte for high-energy rechargeable metallic lithium batteries. *Nat. Commun.* **4**, 1481 (2013).
6. Cha, E., *et al.* 2D MoS2 as an efficient protective layer for lithium metal anodes in high-performance Li-S batteries. *Nat. Nanotechnol.*, **13**, 337–344 (2018).
7. Pang, Q., Liang, X., Kwok, C. Y., Nazar, L. F. Advances in lithium–sulfur batteries based on multifunctional cathodes and electrolytes. *Nat. Energy* **1**, (2016).
8. Xin, S., Guo, Y. G., J., W. L. Nanocarbon Networks for Advanced-Rechargeable Lithium Batteries. *Accounts Chem. Res.* **45**, 1759–1769 (2012).
9. Liu, X., Huang, J. Q., Zhang, Q., Mai, L. Q. Nanostructured Metal Oxides and Sulfides for Lithium-Sulfur Batteries. *Adv. Mater.* **29**, 1601759 (2017).
10. Zu, C., Manthiram, A. Hydroxylated Graphene-Sulfur Nanocomposites for High-Rate Lithium-Sulfur Batteries. *Adv. Energy Mater.* **3**, 1008–1012 (2013).
11. Zhao, M. Q., *et al.* Unstacked double-layer templated graphene for high-rate lithium-sulphur batteries. *Nat. Commun.* **5**, 3410 (2014).
12. Yu, P., *et al.* Advanced Graphene@Sulfur composites via an in-situ reduction and wrapping strategy for high energy density lithium–sulfur batteries. *Carbon* **150**, 224–232 (2019).
13. Tang, C., *et al.* Nitrogen-doped aligned carbon nanotube/graphene sandwiches: facile catalytic growth on bifunctional natural catalysts and their applications as scaffolds for high-rate lithium-sulfur batteries. *Adv. Mater.* **26**, 6100–6105 (2014).
14. Qie, L., Manthiram, A. High-Energy-Density Lithium–Sulfur Batteries Based on Blade-Cast Pure Sulfur Electrodes. *ACS Energy Letters* **1**, 46–51 (2016).
15. Ji, X., Lee, K. T., Nazar, L. F. A highly ordered nanostructured carbon-sulphur cathode for lithium-sulphur batteries. *Nat. Mater.* **8**, 500–506 (2009).
16. Li, Z., *et al.* A Highly Ordered Meso@Microporous Carbon-Supported Sulfur@Smaller Sulfur Core-Shell Structured Cathode for LiS Batteries. *ACS Nano.* **8**, 9295–9303 (2014).
17. Liang, X., Hart, C., Pang, Q., Garsuch, A., Weiss, T., Nazar, L. F. A highly efficient polysulfide mediator for lithium-sulfur batteries. *Nat. Commun.* **6**, 5682 (2015).
18. Zhang, Z.-W., Peng, H.-J., Zhao, M., Huang, J.-Q. Heterogeneous/Homogeneous Mediators for High-Energy-Density Lithium-Sulfur Batteries: Progress and Prospects. *Adv. Funct. Mater.* **28**, 1707536 (2018).

19. Wang, R., *et al.* Highly Dispersed Cobalt Clusters in Nitrogen-Doped Porous Carbon Enable Multiple Effects for High-Performance Li–S Battery. *Adv. Energy Mater.* **10**, 1903550 (2020).
20. Hagen, M., Hanselmann, D., Ahlbrecht, K., Maça, R., Gerber, D., Tübke, J. Lithium-Sulfur Cells: The Gap between the State-of-the-Art and the Requirements for High Energy Battery Cells. *Adv. Energy Mater.* **5**, 1401986 (2015).
21. Ye, Y., Wu, F., Xu, S., Qu, W., Li, L., Chen, R. Designing Realizable and Scalable Techniques for Practical Lithium Sulfur Batteries: A Perspective. *J. Phys. Chem. Lett.* **9**, 1398–1414 (2018).
22. Fang, R., Zhao, S., Sun, Z., Wang, D. W., Cheng, H. M., Li, F. More Reliable Lithium-Sulfur Batteries: Status, Solutions and Prospects. *Adv. Mater.* **29**, 1606823 (2017).
23. Dörfler, S., Althues, H., Härtel, P., Abendroth, T., Schumm, B., Kaskel, S. Challenges and Key Parameters of Lithium-Sulfur Batteries on Pouch Cell Level. *Joule* **4**, 539–554 (2020).
24. Wang, Y., Fu, X., Zheng, M., Zhong, W. H., Cao, G. Strategies for Building Robust Traffic Networks in Advanced Energy Storage Devices: A Focus on Composite Electrodes. *Adv. Mater.* **31**, e1804204 (2019).
25. Chen, W., *et al.* A New Type of Multifunctional Polar Binder: Toward Practical Application of High Energy Lithium Sulfur Batteries. *Adv. Mater.* **29**, 1605160 (2017).
26. Qie, L., Manthiram, A. A facile layer-by-layer approach for high-areal-capacity sulfur cathodes. *Adv. Mater.* **27**, 1694–1700 (2015).
27. Fang, R., *et al.* 3D Interconnected Electrode Materials with Ultrahigh Areal Sulfur Loading for Li-S Batteries. *Adv. Mater.* **28**, 3374–3382 (2016).
28. Liang, X., Rangom, Y., Kwok, C. Y., Pang, Q., Nazar, L. F. Interwoven MXene Nanosheet/Carbon-Nanotube Composites as Li-S Cathode Hosts. *Adv. Mater.* **29**, 1603040 (2017).
29. Lv, D. P., *et al.* High energy density Lithium-Sulfur Batteries: Challenges of Thick Sulfur Cathodes. *Adv. Energy Mater.* **5**, 1402290 (2015).
30. Shi, L., *et al.* Reaction heterogeneity in practical high-energy lithium–sulfur pouch cells. *Energy Environ. Sci.* **13**, 3620–3632 (2020).
31. Yan, P., *et al.* Tailoring grain boundary structures and chemistry of Ni-rich layered cathodes for enhanced cycle stability of lithium-ion batteries. *Nat. Energy* **3**, 600–605 (2018).
32. Liu, W., *et al.* Nickel-rich layered lithium transition-metal oxide for high-energy lithium-ion batteries. *Angew. Chem. Int. Ed.* **54**, 4440–4457 (2015).
33. Sun, Y. K., Myung, S. T., Park, B. C., Prakash, J., Belharouak, I., Amine, K. High-energy cathode material for long-life and safe lithium batteries. *Nat. Mater.* **8**, 320–324 (2009).
34. Li, Z., Guan, B. Y., Zhang, J., Lou, X. W. A Compact Nanoconfined Sulfur Cathode for High-Performance Lithium-Sulfur Batteries. *Joule* **1**, 576–587 (2017).
35. Ye, Y., *et al.* Toward Practical High-Energy Batteries: A Modular-Assembled Oval-Like Carbon Microstructure for Thick Sulfur Electrodes. *Adv Mater* **29**, 1700598 (2017).

36. Kang, N., *et al.* Cathode porosity is a missing key parameter to optimize lithium-sulfur battery energy density. *Nat. Commun.* **10**, 4597 (2019).
37. Liu, Y. T., Liu, S., Li, G. R., Yan, T. Y., CAO, X. P. High Volumetric Energy Density Sulfur Cathode with Heavy and Catalytic Metal Oxide Host for Lithium–Sulfur Battery. *Adv. Sci.* **7**, 1903693 (2020).
38. Lu, D., *et al.* Enabling High-Energy-Density Cathode for Lithium-Sulfur Batteries. *ACS Appl. Mater. Interfaces* **10**, 23094–23102 (2018).
39. Xue, W., *et al.* Intercalation-conversion hybrid cathodes enabling Li–S full-cell architectures with jointly superior gravimetric and volumetric energy densities. *Nat. Energy* **4**, 374–382 (2019).
40. Pang, Q., Liang, X., Kwok, C. Y., Kulisch, J., Nazar, L. F. A Comprehensive Approach toward Stable Lithium–Sulfur Batteries with High Volumetric Energy Density. *Adv. Energy Mater.* **7**, 1601630 (2016).
41. Zheng, J. M., *et al.* Revisit Carbon-Sulfur Composite for Li-S Batteries. *J. Electrochem. Soc.* **160**, A1624-A1628 (2013).

Figures

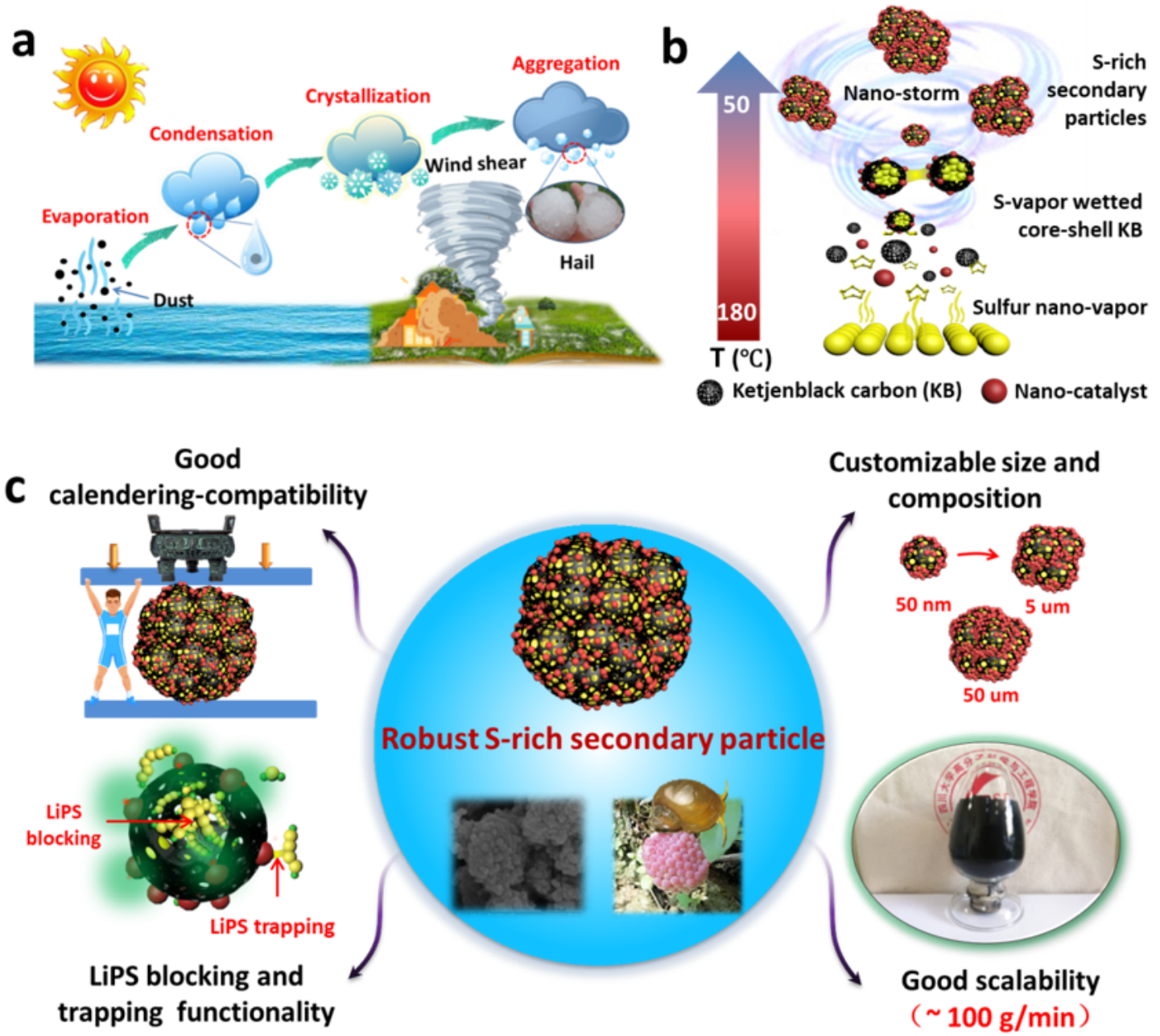

Figure 1

The proposed hail-inspired sulfur nanostorm technology (HSN) for massively producing advanced biomemitic sulfur-rich secondary partilces (SP@HSN) with balanced functions and mechanical properties. a, A schematic of hail formation process in nature. b, The proposed hail-inspired system for producing robust biomemitic sulfur-rich secondary particles. c, Schematic of the design principles for the robust biomimetic secondary particle toward low-cost and high-energy Li-S battery.

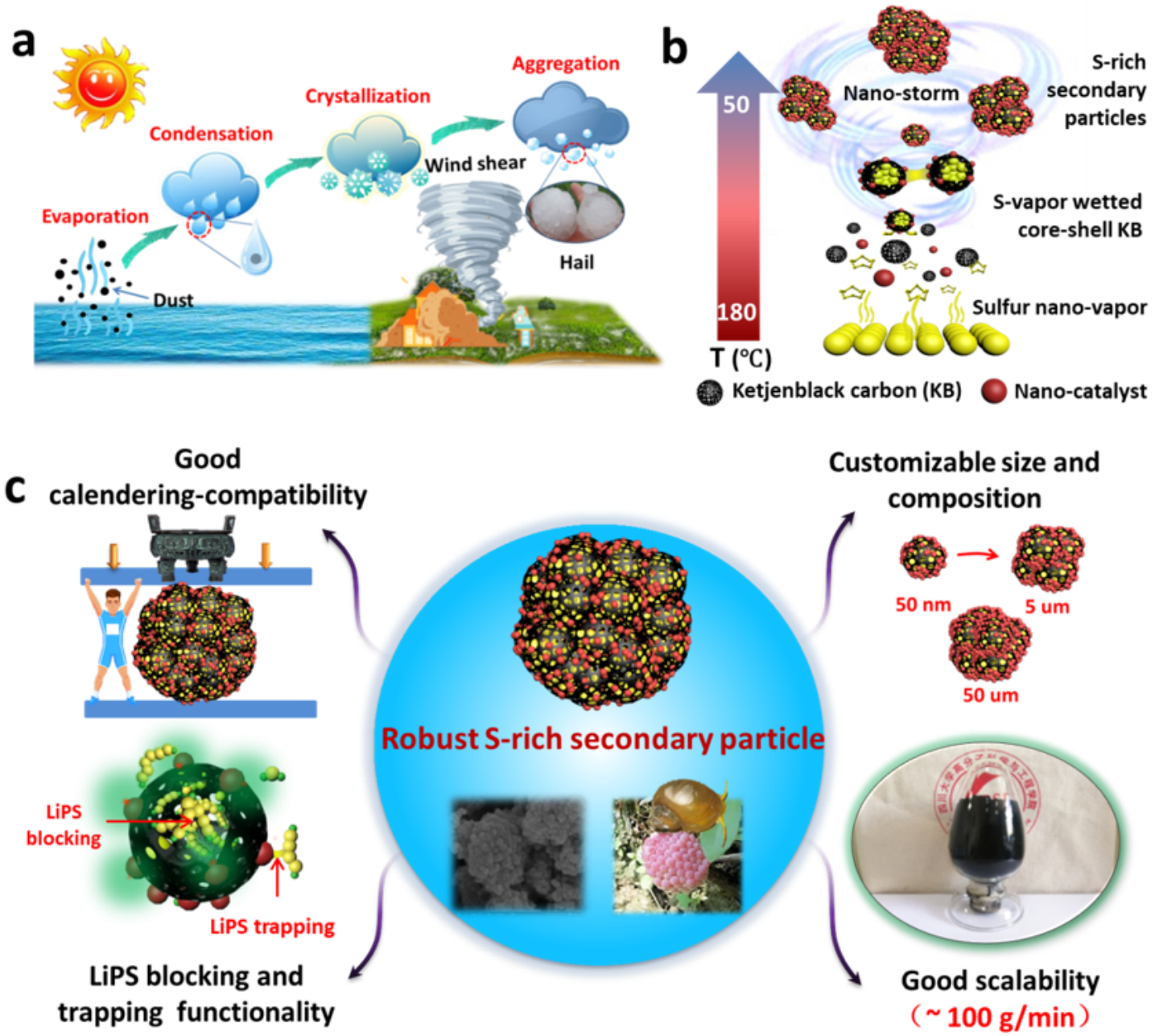

Figure 1

The proposed hail-inspired sulfur nanostorm technology (HSN) for massively producing advanced biomemitic sulfur-rich secondary partilces (SP@HSN) with balanced functions and mechanical properties. a, A schematic of hail formation process in nature. b, The proposed hail-inspired system for producing robust biomemitic sulfur-rich secondary particles. c, Schematic of the design principles for the robust biomimetic secondary particle toward low-cost and high-energy Li-S battery.

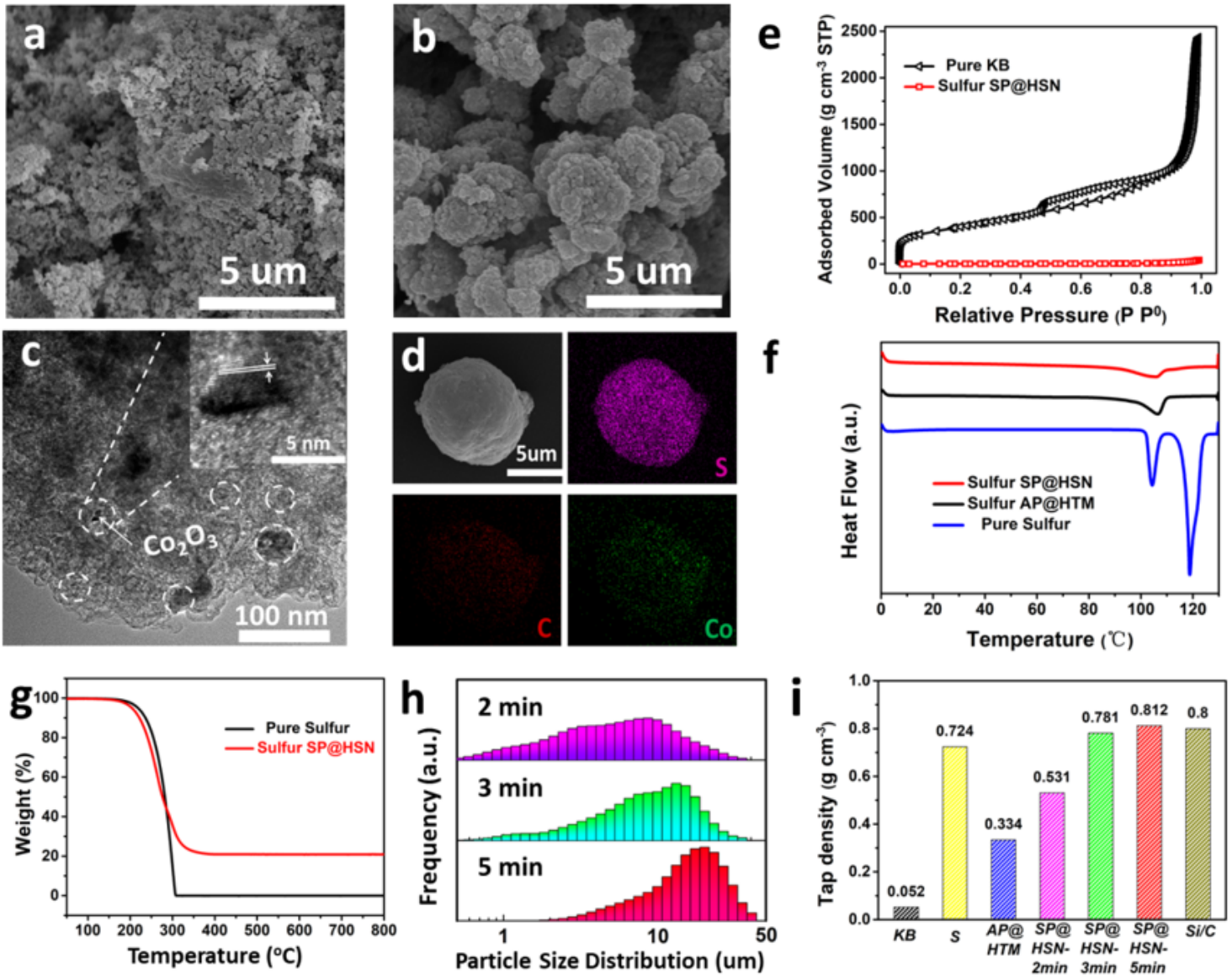

Figure 2

Structrues of the biomimetic sulfur SP@HSN as compared with conventional S/C composites. SEM images of a, sulfur AP@HTM and b, sulfur SP@HSN, scale bar is 5 um. c, TEM image of the sulfur SP@HSN. d, S, C and Co element mapping by Energy-dispersive X-ray for single secondary particle. e, N2 sorption isotherms of pure KB and sulfur SP@HSN. f, The first heating curves by DSC for pure sulfur, sulfur AP@HTM and sulfur SP@HSN. g, Thermogravimetric analysis curves of pure sulfur and sulfur SP@HSN. h, Size regulation of the sulfur SP@HSN by compositing time: 2 min (top), 3 min (middle) , 5 min (bottom). i, Comparison of the tap desnity of the sulfur SP@HSN with other electrode particles.

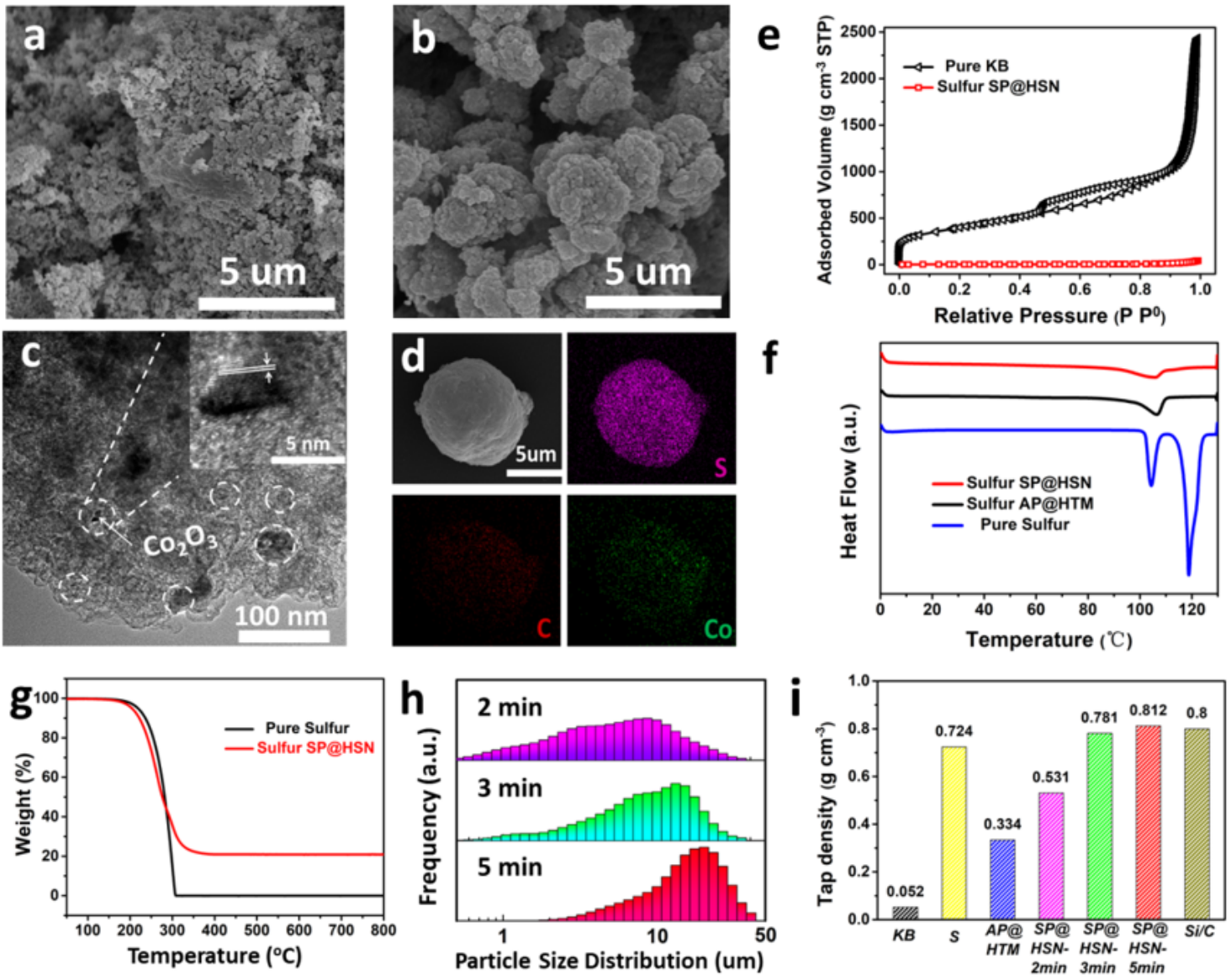

Figure 2

Structrues of the biomimetic sulfur SP@HSN as compared with conventional S/C composites. SEM images of a, sulfur AP@HTM and b, sulfur SP@HSN, scale bar is 5 um. c, TEM image of the sulfur SP@HSN. d, S, C and Co element mapping by Energy-dispersive X-ray for single secondary particle. e, N2 sorption isotherms of pure KB and sulfur SP@HSN. f, The first heating curves by DSC for pure sulfur, sulfur AP@HTM and sulfur SP@HSN. g, Thermogravimetric analysis curves of pure sulfur and sulfur SP@HSN. h, Size regulation of the sulfur SP@HSN by compositing time: 2 min (top), 3 min (middle) , 5 min (bottom). i, Comparison of the tap desnity of the sulfur SP@HSN with other electrode particles.

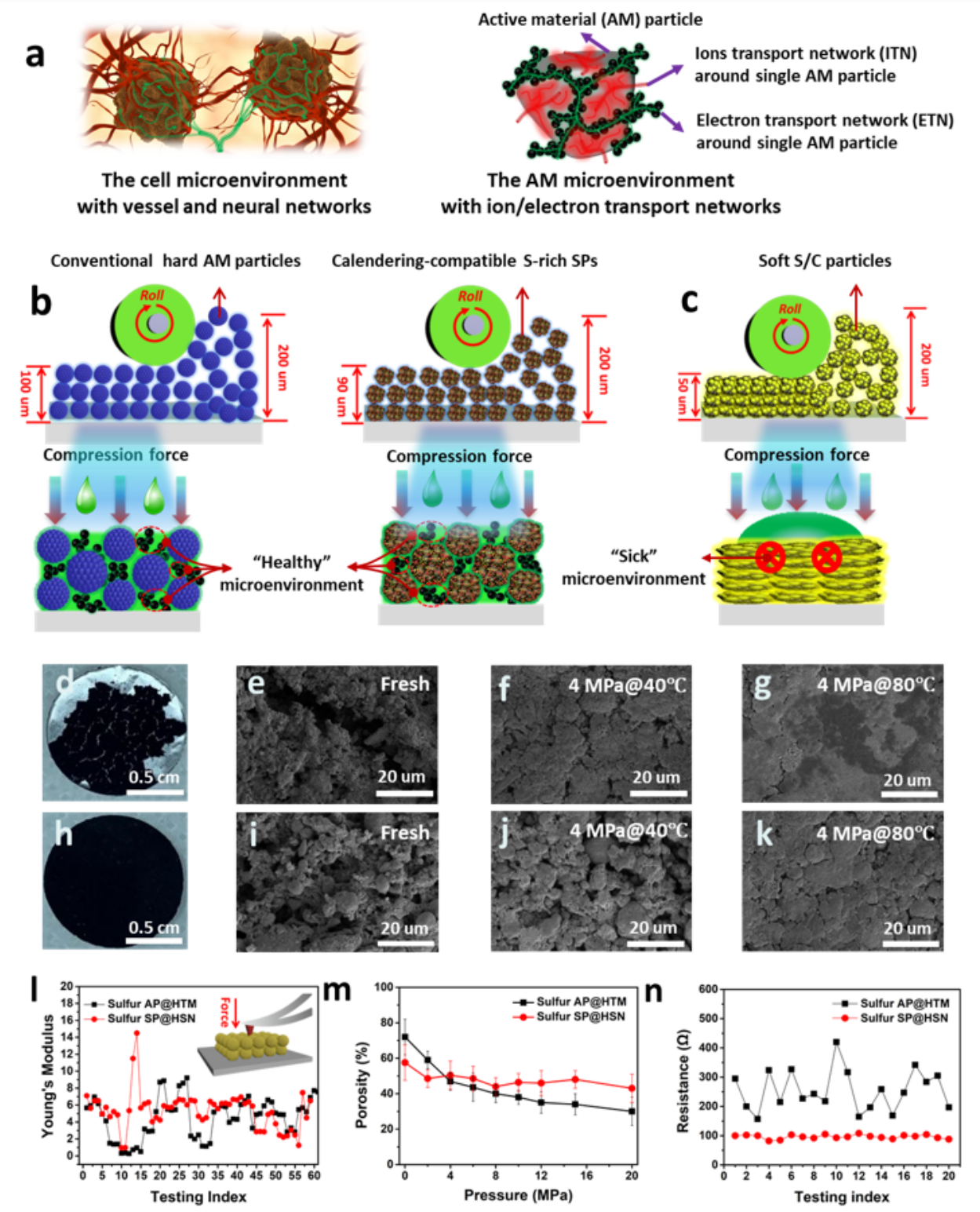

Figure 3

The calendering-compatibility of S-rich SP@HSN and its role in controlling the AM microenvironment inside composite electrodes. a, Illustration of the cell microenvironment in biology and the concept of AM microenviroment in composite electrodes. b, c, Schematic of the role of AM mechanical properties in controlling the AM microenvironment during calendering process for hard AM (NCM electrode and the sulfur SP@HSN electrode) and soft AM (sulfur AP@HTM electrode), respectively. d, e, Digital photo and

SEM image of the sulfur AP@HTM electrode. f, g, SEM images of the sulfur AP@HTM electrode after 4 MPa compression treatment at 40 and 80 °C, respectively. h,i, Digital photo and SEM image of the sulfur SP@HSN electrode. j, k, SEM images of the sulfur SP@HSN electrode after 4 MPa compression treatment at 40 and 80 °C, respectively. l, Comparison of the apparent compression modulus for sulfur AP@HTM and sulfur SP@HSN particles. m, Comparsion of the electrode porosity for sulfur AP@HTM and sulfur SP@HSN under various perssure. n, Point mapping of electronic resistance for the sulfur AP@HTM and sulfur SP@HSN cathodes.

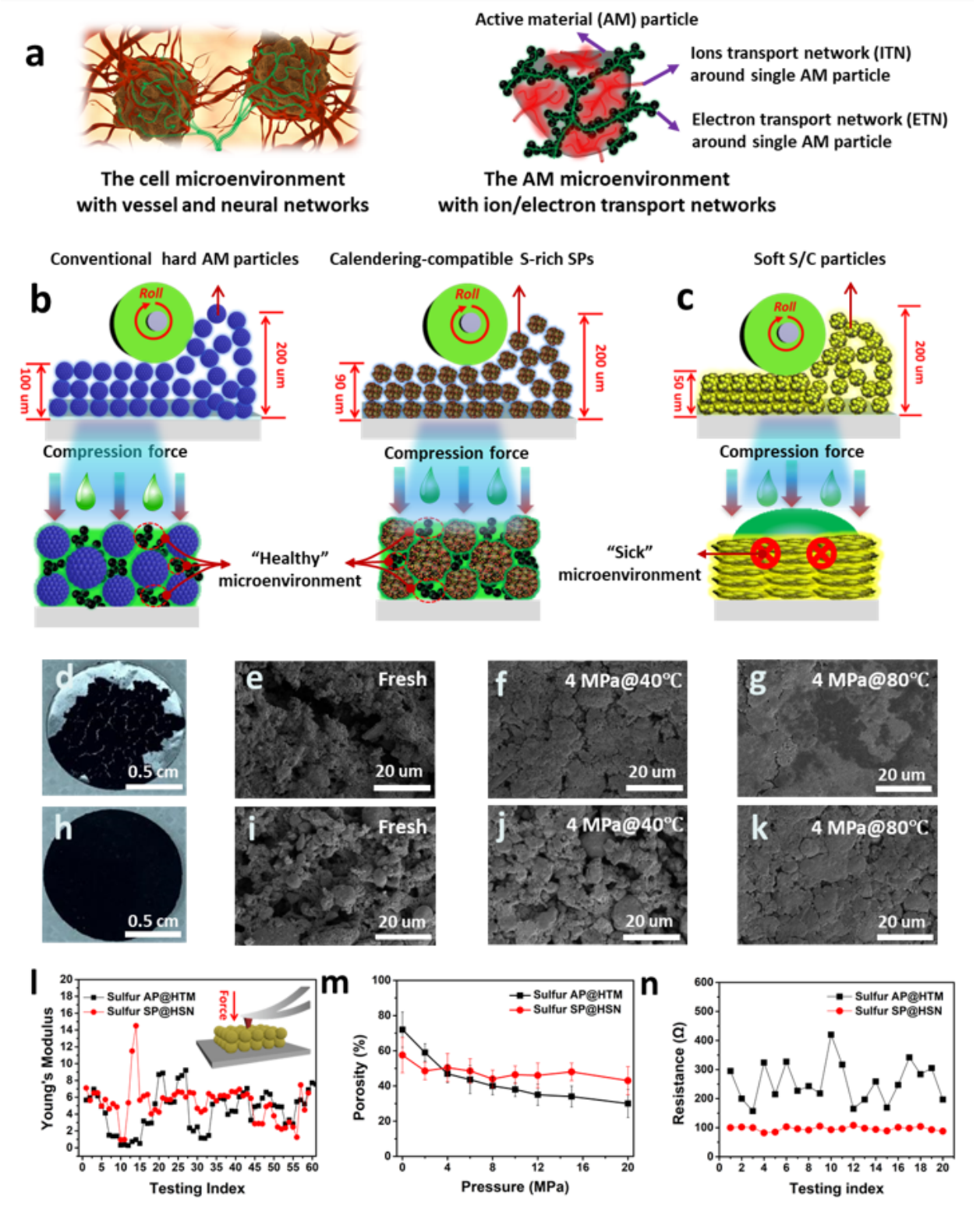

Figure 3

The calendering-compatibility of S-rich SP@HSN and its role in controlling the AM microenvironment inside composite electrodes. a, Illustration of the cell microenvironment in biology and the concept of AM microenviroment in composite electrodes. b, c, Schematic of the role of AM mechanical properties in controlling the AM microenvironment during calendering process for hard AM (NCM electrode and the sulfur SP@HSN electrode) and soft AM (sulfur AP@HTM electrode), respectively. d, e, Digital photo and SEM image of the sulfur AP@HTM electrode. f, g, SEM images of the sulfur AP@HTM electrode after 4 MPa compression treatment at 40 and 80 ℃, respectively. h,i, Digital photo and SEM image of the sulfur SP@HSN electrode. j, k, SEM images of the sulfur SP@HSN electrode after 4 MPa compression treatment at 40 and 80 ℃, respectively. l, Comparison of the apparent compression modulus for sulfur AP@HTM and sulfur SP@HSN particles. m, Comparsion of the electrode porosity for sulfur AP@HTM and sulfur SP@HSN under various perssure. n, Point mapping of electronic resistance for the sulfur AP@HTM and sulfur SP@HSN cathodes.

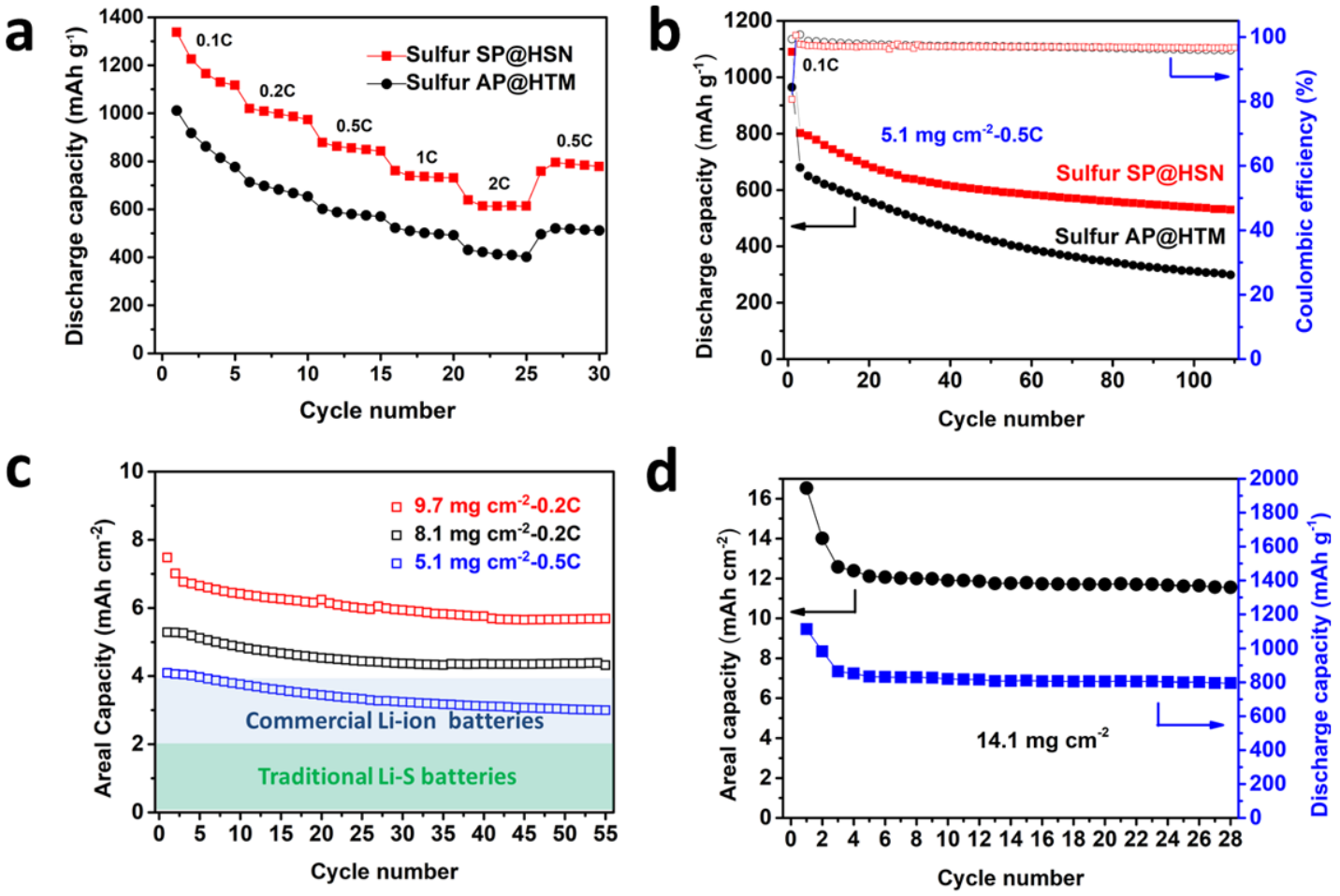

Figure 4

Electrochemical performance of SP@HSN Li-S battery evaluated in coin cell condition. a, Comparison of C-rate performance between sulfur SP@HSN and sulfur AP@HTM cthodes. b, Comparison of cycle

performance of sulfur SP@HSN and sulfur AP@HTM cathodes with a sulfur loading of 5.1 mg cm-2 at 0.5 C. c, Cycle performance of sulfur SP@HSN cathodes with sulfur loading of 5.1 mg cm-2 at 0.5C, 8.1 and 9.7 mg cm-2 at 0.2 C. d, Stable cycling of sulfur SP@HSN cathodes with a high sulfur loading of 14.1 mg cm-2 at 1 mA cm-2.

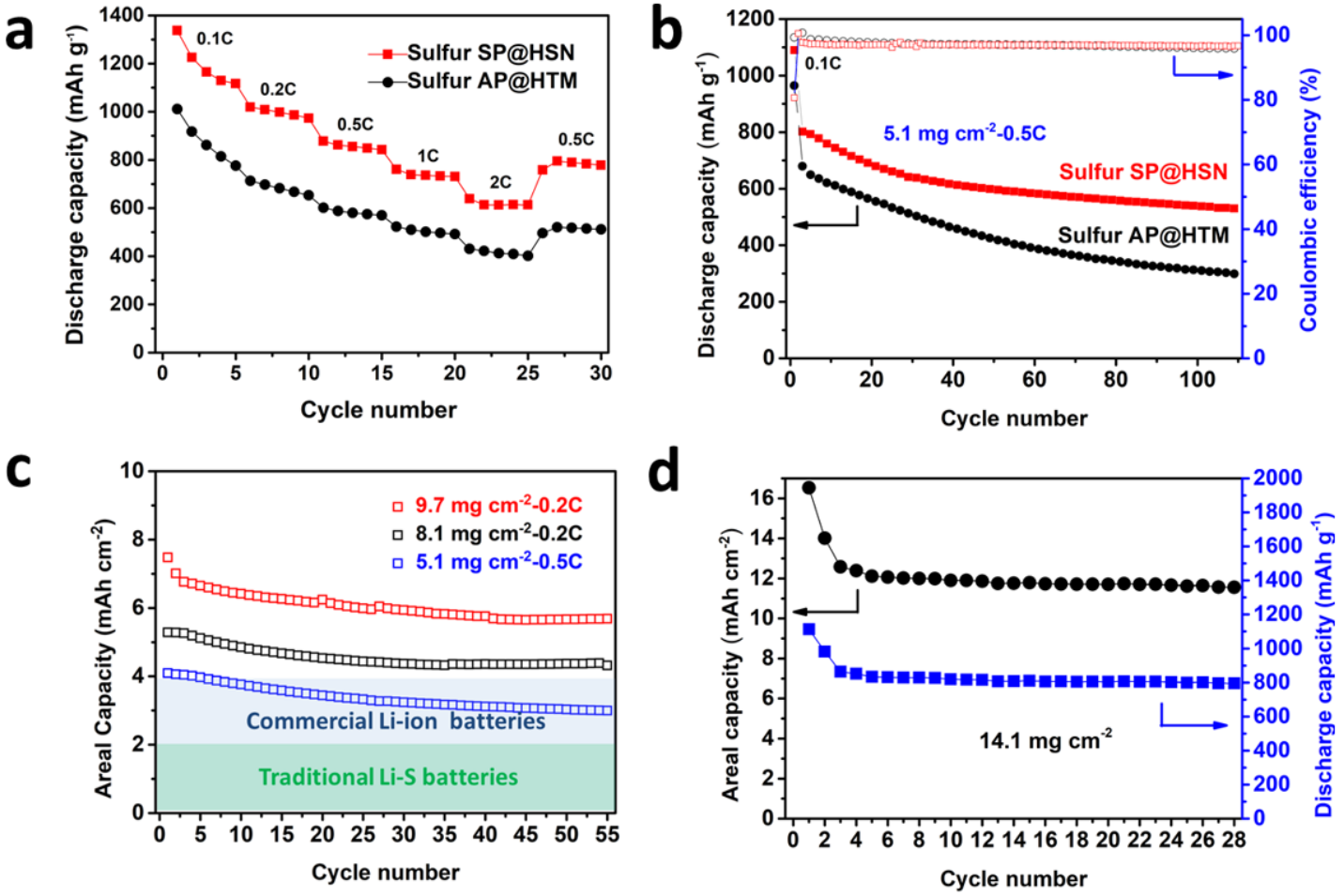

Figure 4

Electrochemical performance of SP@HSN Li-S battery evaluated in coin cell condition. a, Comparison of C-rate performance between sulfur SP@HSN and sulfur AP@HTM cthodes. b, Comparison of cycle performance of sulfur SP@HSN and sulfur AP@HTM cathodes with a sulfur loading of 5.1 mg cm-2 at 0.5 C. c, Cycle performance of sulfur SP@HSN cathodes with sulfur loading of 5.1 mg cm-2 at 0.5C, 8.1 and 9.7 mg cm-2 at 0.2 C. d, Stable cycling of sulfur SP@HSN cathodes with a high sulfur loading of 14.1 mg cm-2 at 1 mA cm-2.

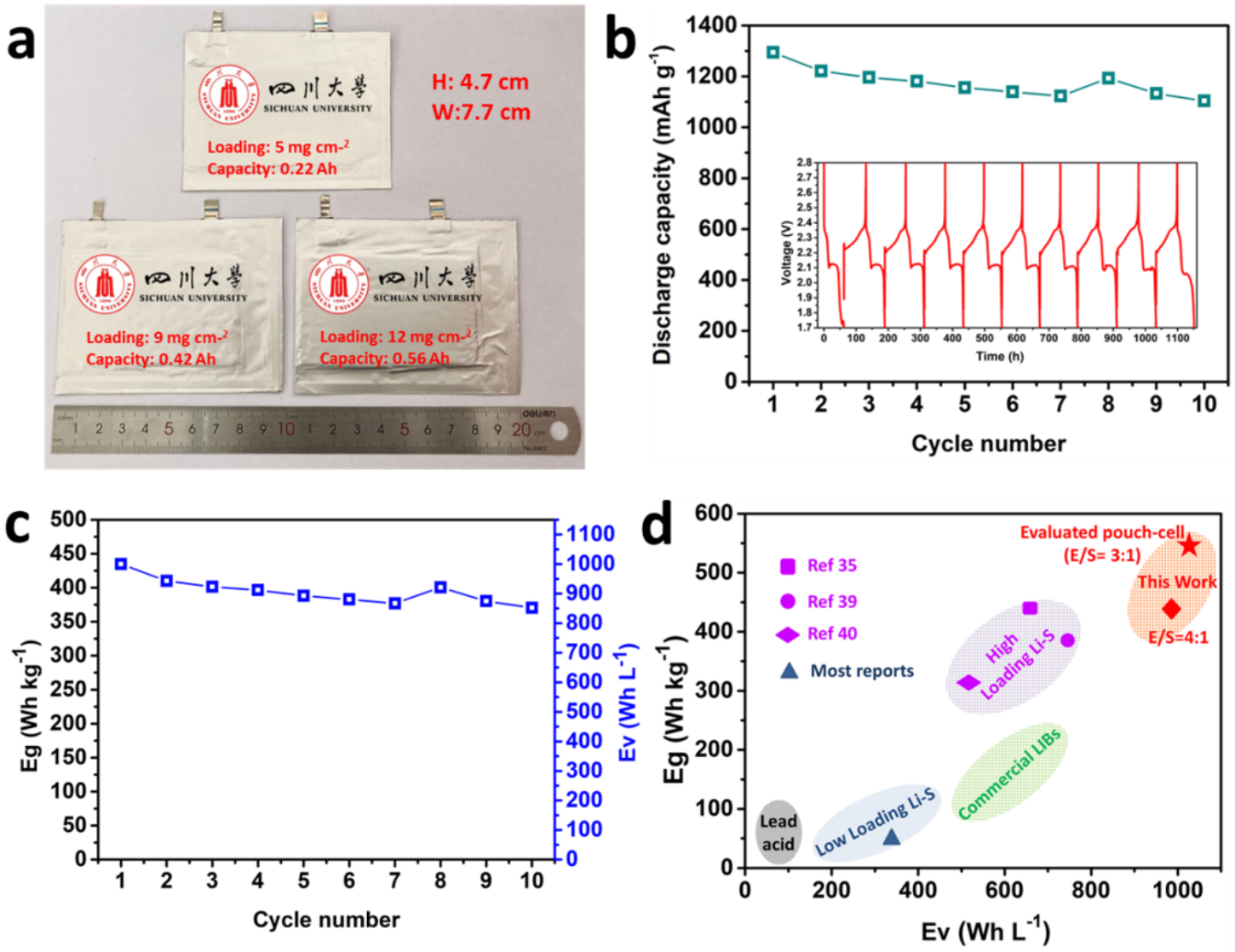

Figure 5

Electrochemical performance of the SP@HSN Li-S battery in pouch cell condition. a, The digital photograph of Li-S pouch cells (4.7 cm × 7.7 cm) aseembled with various loading of sulfur SP@HSN. b, The discharge capacity and discharge/charge profiles for a pouch cell with a S-loading of 12 mg cm-2. c, The gravimetric (Eg) and volumetric (Ev) energy densities for this pouch cell. d, Comparsion of the energy density of this work with those from representive literatures.

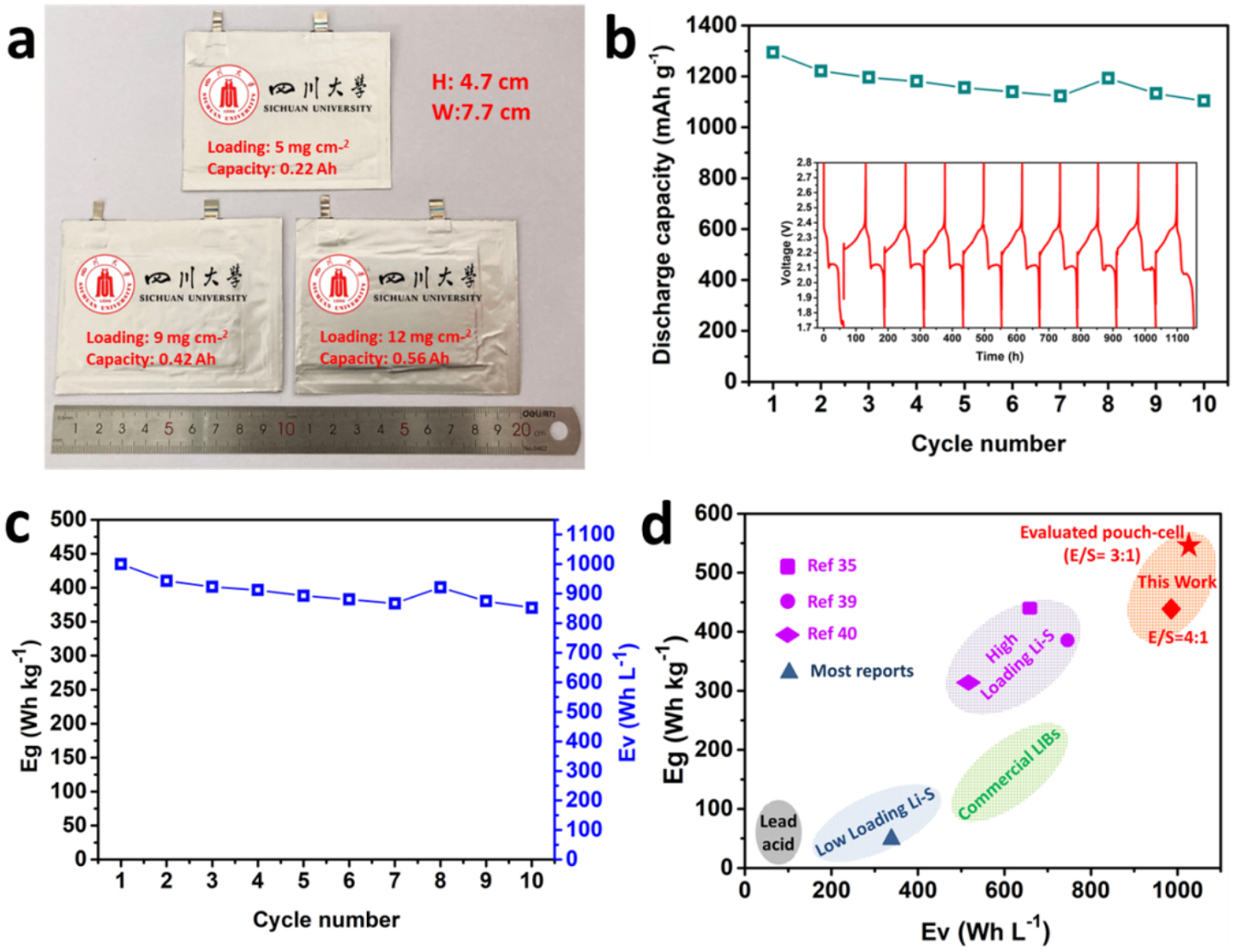

Figure 5

Electrochemical performance of the SP@HSN Li-S battery in pouch cell condition. a, The digital photograph of Li-S pouch cells (4.7 cm □ 7.7 cm) aseembled with various loading of sulfur SP@HSN. b, The discharge capacity and discharge/charge profiles for a pouch cell with a S-loading of 12 mg cm-2. c, The gravimetric (Eg) and volumetric (Ev) energy densities for this pouch cell. d, Comparsion of the energy density of this work with those from representive literatures.

Supplementary Files

This is a list of supplementary files associated with this preprint. Click to download.

- VideoS1.mp4
- VideoS1.mp4

- SI.docx
- SI.docx
- VideoS2.mp4
- VideoS2.mp4
- TOC.png
- TOC.png